A Three-Dimensional Haar-Wavelet-Based Multiresolution Analysis Similar to the FDTD Method—Derivation and Application

Masafumi Fujii, *Student Member, IEEE*, and Wolfgang J. R. Hoefer, *Fellow, IEEE*

***Abstract*— A three-dimensional (3-D) multiresolution analysis procedure similar to the finite-difference time-domain (FDTD) method is derived using a complete set of three-dimensional orthonormal bases of Haar scaling and wavelet functions. The expansion of the electric and the magnetic fields in these basis functions leads to the time iterative difference approximation of Maxwell's equations that is similar to the FDTD method. This technique effectively models realistic microwave passive components by virtue of its multiresolution property; the computational time is reduced approximately by half compared to the FDTD method. The proposed technique is validated by analyzing several 3-D rectangular resonators with inhomogeneous dielectric loading. It is also applied to the analyses of microwave passive devices with open boundaries such as micrstrip low-pass filters and spiral inductors to extract their S-parameters and field distributions. The results of the proposed technique agree well with those of the traditional FDTD method.**

***Index Terms*— FDTD method, Haar wavelets, multiresolution analysis.**

I. Introduction

NUMERICAL computation has become a powerful and important technique for solving electromagnetic problems. This is due to increased computer performance as well as to growing complexity of problems that must be solved. Time domain methods such as finite-difference time-domain (FDTD) [1] and transmission line matrix (TLM) [2] methods are gaining importance by virtue of their versatility and the natural way in which they simulate what happens in reality. Nevertheless, these methods are limited by available computer memory and computational time.

In the meantime, wavelet analysis has been vigorously studied in the field of mathematics [3], [4]. It has been reported that wavelet analysis can be applied to frequency-domain electromagnetic analysis via the method of moments to improve computational efficiencies due to the orthonormal and multiresolutional nature of the wavelet functions [5].

The following time-domain techniques have recently been proposed to improve computational efficiency: the Battle–Lemarie-wavelet-based multiresolution time-domain (MRTD) technique [6], [7], the Daubechies-wavelet-based technique [8], and a multigrid technique using Haar wavelets [9], [10]. These techniques have been applied to analyze three-dimensional (3-D) cavity resonator problems [7], [11], two-dimensional field distributions in microstrip lines [9], [12], and three-dimensional cavities with various inhomogeneous dielectrics [13]. Although these techniques have complex dispersion properties [14], it has been pointed out that they have the advantage of requiring less computational effort than other time-domain techniques.

This paper describes the derivation and the application of an FDTD-like multiresolution technique based on Haar wavelets. It is formulated in three-dimensional space and time using Haar scaling and wavelet functions at one scaling level. A complete set of orthonormal bases in three-dimensional real-space is first created using Haar scaling and wavelet functions. The field components in the E–H formulation of Maxwell's equations are then expanded in the orthonormal bases. Subsequently following Galerkin's procedure of the method of moments, it leads to FDTD-like time-iterative difference equations that are individually applied to each basis function. For structures with inhomogeneous dielectric materials, dielectric materials are treated in an approximate manner where the relative permittivity has an isotropic property at the interfaces of different dielectric materials. An exact treatment for analyzing inhomogeneous dielectric materials will be discussed in the last section; this exact formulation leads to a stable algorithm. The perfect electric conductor (PEC) boundaries are first formulated using simple forward- or backward-difference approximation. The PEC boundaries are then improved by using Lagrange interpolation to analyze higher order modes in a cavity. Mur's first-order absorbing boundary condition (ABC) is implemented in this paper. ABC's can be implemented similarly as in the conventional FDTD method. In the case of the Haar scaling and wavelet basis functions, a basis transformation matrix was found to be useful for sampling field values from wavelet expansion coefficients.

Several rectangular cavities with inhomogeneous dielectric loading were analyzed to validate the proposed technique. The results were then compared with analytical results (when available) and with data obtained by a conventional FDTD

Manuscript received March 27, 1998; revised September 3, 1998.

The authors are with the Department of Electrical and Computer Engineering, University of Victoria, Victoria, B.C. Canada V8W 3P6 (e-mail: fujii@ece.uvic.ca).

Publisher Item Identifier S 0018-9480(98)09186-8.

analysis having the same number of degrees of freedom; the comparison was under a condition that the same amount of computer memory was involved in both methods. Furthermore, the proposed technique is also applied to analyze microstrip low-pass filters and spiral inductors with open boundaries to extract their S-parameters and field distributions. The results were compared to those obtained with the conventional FDTD analysis. These analyses demonstrate the suitability of this new technique for solving practical microwave problems.

The required computer resources are discussed and compared with those of the conventional FDTD method. The multiresolution technique has a potential capability of reducing the computational effort by thresholding small coefficients [11]; the unknown coefficients that are smaller than a certain value can be omitted without affecting the computational accuracy. However, thresholding has not been implemented in this paper. Although the accuracy and the memory requirement of this new procedure are similar to those of a conventional FDTD method having the same number of degrees of freedom, the multiresolution technique based on Haar wavelets is approximately twice as fast.

II. Formulation

A. 3-D Basis Functions and Time Iterative Difference Equations

The field components in Maxwell's curl equations

$$\nabla \times \mathbf{E} = -\mu \frac{\partial \mathbf{H}}{\partial t} \tag{1a}$$

$$\nabla \times \mathbf{H} = \epsilon \frac{\partial \mathbf{E}}{\partial t} + \sigma \mathbf{E} + \mathbf{J} \tag{1b}$$

are expanded in the following eight orthonormal basis functions. Those basis functions are products of three-dimensional combinations of the Haar scaling (ϕ) and wavelet (ψ) functions [3] multiplied by a rectangular pulse function in time (h) as follows:

$$\begin{cases} \phi_i(x)\phi_j(y)\phi_k(z)h_n(t) \\ \phi_i(x)\phi_j(y)\psi_k(z)h_n(t) \\ \phi_i(x)\psi_j(y)\phi_k(z)h_n(t) \\ \psi_i(x)\phi_j(y)\phi_k(z)h_n(t) \\ \phi_i(x)\psi_j(y)\psi_k(z)h_n(t) \\ \psi_i(x)\phi_j(y)\psi_k(z)h_n(t) \\ \psi_i(x)\psi_j(y)\phi_k(z)h_n(t) \\ \psi_i(x)\psi_j(y)\psi_k(z)h_n(t) \end{cases} \tag{2}$$

where

$$\phi_m(w) = \phi\left(\frac{w - m\Delta w}{\Delta w}\right) \tag{3a}$$

$$\psi_m(w) = \psi\left(\frac{w - m\Delta w}{\Delta w}\right), \tag{3b}$$

$$\text{for } (w, m) = (x, i), (y, j), (z, k)$$

and

$$h_n(t) = \begin{cases} 1, & \text{for } (n - 1/2)\Delta t \le t < (n + 1/2)\Delta t \\ 0, & \text{otherwise} \end{cases} \tag{4}$$

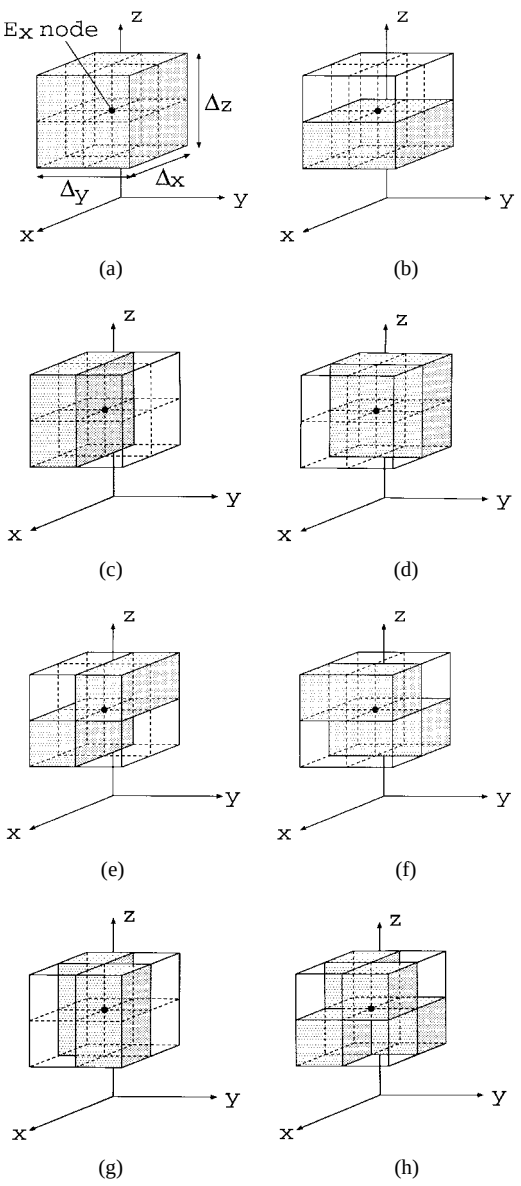

Fig. 1. Three-dimensional Haar basis functions for an E_x node. Hatched regions represent $+1$ and unhatched regions represent -1.

with the space and time discretization intervals Δx, Δy, Δz, and Δt. Instead of the definition of ϕ and ψ in [3], the following must be used to obtain appropriate inner products when applying Galerkin's procedure as described later

$$\phi(s) = \begin{cases} 1, & \text{for } |s| < 1/2 \\ 1/2, & \text{for } |s| = 1/2 \\ 0, & \text{otherwise} \end{cases} \tag{5a}$$

$$\psi(s) = \begin{cases} 1/2, & \text{for } s = -1/2 \\ 1, & \text{for } -1/2 < s < 0 \\ -1, & \text{for } 0 < s < 1/2 \\ -1/2, & \text{for } s = 1/2 \\ 0, & \text{for } s = 0 \text{ and otherwise.} \end{cases} \tag{5b}$$

The basis functions (2) have the support (or the width of the function having nonzero value) equal to the spatial discretization intervals Δx, Δy, and Δz. The spatial basis functions for an E_x node are shown as an example in Fig. 1.

In Cartesian coordinates, the expansions of the electric field and the current density, E_x and J_x for example, are given by

$$\begin{aligned} F_x(\vec{r},t) = &\sum_{i=0}^{I}\sum_{j=0}^{J}\sum_{k=0}^{K}\sum_{n=0}^{N} h_n(t) \\ &\cdot\Big\{ {}^{x}_{n}F^{\phi\phi\phi}_{i+1/2,\,j,\,k}\,\phi_{i+1/2}(x)\,\phi_j(y)\,\phi_k(z) \\ &+ {}^{x}_{n}F^{\phi\phi\psi}_{i+1/2,\,j,\,k}\,\phi_{i+1/2}(x)\,\phi_j(y)\,\psi_k(z) \\ &+ {}^{x}_{n}F^{\phi\psi\phi}_{i+1/2,\,j,\,k}\,\phi_{i+1/2}(x)\,\psi_j(y)\,\phi_k(z) \\ &+ {}^{x}_{n}F^{\psi\phi\phi}_{i+1/2,\,j,\,k}\,\psi_{i+1/2}(x)\,\phi_j(y)\,\phi_k(z) \\ &+ {}^{x}_{n}F^{\phi\psi\psi}_{i+1/2,\,j,\,k}\,\phi_{i+1/2}(x)\,\psi_j(y)\,\psi_k(z) \\ &+ {}^{x}_{n}F^{\psi\phi\psi}_{i+1/2,\,j,\,k}\,\psi_{i+1/2}(x)\,\phi_j(y)\,\psi_k(z) \\ &+ {}^{x}_{n}F^{\psi\psi\phi}_{i+1/2,\,j,\,k}\,\psi_{i+1/2}(x)\,\psi_j(y)\,\phi_k(z) \\ &+ {}^{x}_{n}F^{\psi\psi\psi}_{i+1/2,\,j,\,k}\,\psi_{i+1/2}(x)\,\psi_j(y)\,\psi_k(z)\Big\}, \\ &\text{for } F = E \text{ and } J \end{aligned} \tag{6}$$

and the expansion of the magnetic field, H_x for example, is given by

$$\begin{aligned} &H_x(\vec{r},t) \\ &= \sum_{i=0}^{I}\sum_{j=0}^{J}\sum_{k=0}^{K}\sum_{n=0}^{N} h_{n+1/2}(t) \\ &\cdot\Big\{ {}_{n+1/2}{}^{x}H^{\phi\phi\phi}_{i,\,j+1/2,\,k+1/2}\,\phi_i(x)\,\phi_{j+1/2}(y)\,\phi_{k+1/2}(z) \\ &+ {}_{n+1/2}{}^{x}H^{\phi\phi\psi}_{i,\,j+1/2,\,k+1/2}\,\phi_i(x)\,\phi_{j+1/2}(y)\,\psi_{k+1/2}(z) \\ &+ {}_{n+1/2}{}^{x}H^{\phi\psi\phi}_{i,\,j+1/2,\,k+1/2}\,\phi_i(x)\,\psi_{j+1/2}(y)\,\phi_{k+1/2}(z) \\ &+ {}_{n+1/2}{}^{x}H^{\psi\phi\phi}_{i,\,j+1/2,\,k+1/2}\,\psi_i(x)\,\phi_{j+1/2}(y)\,\phi_{k+1/2}(z) \\ &+ {}_{n+1/2}{}^{x}H^{\phi\psi\psi}_{i,\,j+1/2,\,k+1/2}\,\phi_i(x)\,\psi_{j+1/2}(y)\,\psi_{k+1/2}(z) \\ &+ {}_{n+1/2}{}^{x}H^{\psi\phi\psi}_{i,\,j+1/2,\,k+1/2}\,\psi_i(x)\,\phi_{j+1/2}(y)\,\psi_{k+1/2}(z) \\ &+ {}_{n+1/2}{}^{x}H^{\psi\psi\phi}_{i,\,j+1/2,\,k+1/2}\,\psi_i(x)\,\psi_{j+1/2}(y)\,\phi_{k+1/2}(z) \\ &+ {}_{n+1/2}{}^{x}H^{\psi\psi\psi}_{i,\,j+1/2,\,k+1/2}\,\psi_i(x)\,\psi_{j+1/2}(y)\,\psi_{k+1/2}(z)\Big\} \end{aligned} \tag{7}$$

where the notations are consistent with those used in [7] except that the field value ${}^{x}_{n}F^{\zeta\eta\xi}_{i,\,j,\,k}$ with $F = E, J, H$ and $\zeta, \eta, \xi = \phi, \psi$ denotes the expansion coefficients in terms of the Haar scaling and wavelet functions at time step n and position (i, j, k). The remaining field components can be expanded similarly.

Subsequently, each component is substituted in Maxwell's equations (1), and then, by following Galerkin's procedure of the method of moment, the resulting expressions are tested with the basis functions (2). This leads to time iterative difference equations in terms of the voltage across the E-node ${}^{x}_{n}V^{\zeta\eta\xi}_{i,\,j,\,k} \equiv {}^{x}_{n}E^{\zeta\eta\xi}_{i,\,j,\,k}\,\Delta x$, the current flowing at the H-node ${}^{x}_{n}I^{\zeta\eta\xi}_{i,\,j,\,k} \equiv {}^{x}_{n}H^{\zeta\eta\xi}_{i,\,j,\,k}\,\Delta x$, and the current source at the E-node ${}^{x}_{n}\hat{I}^{\zeta\eta\xi}_{i,\,j,\,k} \equiv {}^{x}_{n}J^{\zeta\eta\xi}_{i,\,j,\,k}\,\Delta y\Delta z$, with x, y, z cyclic and $\zeta, \eta, \xi = \phi, \psi$ as

$$\begin{aligned} {}^{x}_{h}I^{\zeta\eta\xi}_{0h\bar{h}} = &{}^{x}_{\bar{h}}I^{\zeta\eta\xi}_{0h\bar{h}} + {}^{x}C^{m}_{0h\bar{h}} \\ &\cdot\Big\{ {}^{z}_{0}V^{\zeta\eta\xi}_{01\bar{h}} - {}^{z}_{0}V^{\zeta\eta\xi}_{00\bar{h}} - ({}^{y}_{0}V^{\zeta\eta\xi}_{0h1} - {}^{y}_{0}V^{\zeta\eta\xi}_{0h0})\Big\} \end{aligned} \tag{8a}$$

$$\begin{aligned} {}^{y}_{h}I^{\zeta\eta\xi}_{h0\bar{h}} = &{}^{y}_{\bar{h}}I^{\zeta\eta\xi}_{h0\bar{h}} + {}^{y}C^{m}_{h0\bar{h}} \\ &\cdot\Big\{ {}^{x}_{0}V^{\zeta\eta\xi}_{h01} - {}^{x}_{0}V^{\zeta\eta\xi}_{h00} - ({}^{z}_{0}V^{\zeta\eta\xi}_{10\bar{h}} - {}^{z}_{0}V^{\zeta\eta\xi}_{00\bar{h}})\Big\} \end{aligned} \tag{8b}$$

$$\begin{aligned} {}^{z}_{h}I^{\zeta\eta\xi}_{hh0} = &{}^{z}_{\bar{h}}I^{\zeta\eta\xi}_{hh0} + {}^{z}C^{m}_{hh0} \\ &\cdot\Big\{ {}^{y}_{0}V^{\zeta\eta\xi}_{1h0} - {}^{y}_{0}V^{\zeta\eta\xi}_{0h0} - ({}^{x}_{0}V^{\zeta\eta\xi}_{h10} - {}^{x}_{0}V^{\zeta\eta\xi}_{h00})\Big\} \end{aligned} \tag{8c}$$

and

$$\begin{aligned} {}^{x}_{1}V^{\zeta\eta\xi}_{h00} = &{}^{x}C^{0}_{h00}\,{}^{x}_{0}V^{\zeta\eta\xi}_{h00} + {}^{x}C^{e}_{h00}\cdot\Big\{ {}^{z}_{h}I^{\zeta\eta\xi}_{hh0} - {}^{z}_{\bar{h}}I^{\zeta\eta\xi}_{\bar{h}h0} \\ &-({}^{y}_{h}I^{\zeta\eta\xi}_{h0h} - {}^{y}_{h}I^{\zeta\eta\xi}_{h0\bar{h}}) - {}^{x}_{h}\hat{I}^{\zeta\eta\xi}_{h00}\Big\} \end{aligned} \tag{9a}$$

$$\begin{aligned} {}^{y}_{1}V^{\zeta\eta\xi}_{0h0} = &{}^{y}C^{0}_{0h0}\,{}^{y}_{0}V^{\zeta\eta\xi}_{0h0} + {}^{y}C^{e}_{0h0}\cdot\Big\{ {}^{x}_{h}I^{\zeta\eta\xi}_{0hh} - {}^{x}_{\bar{h}}I^{\zeta\eta\xi}_{0\bar{h}h} \\ &-({}^{z}_{h}I^{\zeta\eta\xi}_{hh0} - {}^{z}_{\bar{h}}I^{\zeta\eta\xi}_{\bar{h}h0}) - {}^{y}_{h}\hat{I}^{\zeta\eta\xi}_{0h0}\Big\} \end{aligned} \tag{9b}$$

$$\begin{aligned} {}^{z}_{1}V^{\zeta\eta\xi}_{00h} = &{}^{z}C^{0}_{00h}\,{}^{z}_{0}V^{\zeta\eta\xi}_{00h} + {}^{z}C^{e}_{00h}\cdot\Big\{ {}^{y}_{h}I^{\zeta\eta\xi}_{h0h} - {}^{y}_{\bar{h}}I^{\zeta\eta\xi}_{\bar{h}0h} \\ &-({}^{x}_{h}I^{\zeta\eta\xi}_{0hh} - {}^{x}_{\bar{h}}I^{\zeta\eta\xi}_{0\bar{h}h}) - {}^{z}_{h}\hat{I}^{\zeta\eta\xi}_{00h}\Big\} \end{aligned} \tag{9c}$$

where the left hand side subscripts 0, h, $\bar{h}$, and 1 denote n, $n+1/2$, $n-1/2$, and $n+1$, respectively, and the right hand side subscript, for example, $(h0\bar{h})$ denotes $(i+1/2,\, j,\, k-1/2)$, and so forth. The coefficients are given by

$${}^{x}C^{m}_{ijk} = -\frac{\Delta t}{\mu_{ijk}}\cdot\left[\frac{\Delta x}{\Delta y\,\Delta z}\right]_{ijk} \tag{10a}$$

$${}^{x}C^{0}_{ijk} = \frac{2\epsilon_{ijk} - \sigma_{ijk}\Delta t}{2\epsilon_{ijk} + \sigma_{ijk}\Delta t} \tag{10b}$$

$${}^{x}C^{e}_{ijk} = \frac{2\Delta t}{2\epsilon_{ijk} + \sigma_{ijk}\Delta t}\cdot\left[\frac{\Delta x}{\Delta y\,\Delta z}\right]_{ijk} \tag{10c}$$

for x, y, and z cyclic. The material constants μ_{ijk}, ϵ_{ijk}, and σ_{ijk} are defined as a common value in a unit Yee cell. Equations (8)–(10) are the same as those appearing in the traditional FDTD method. The only difference is that in the multiresolution method, the equations are computed independently for each basis function (2).

B. Relation Between the Haar Basis Coefficients and the Actual Field Values

In this multiresolution technique, the space is discretized using the conventional Yee cell. However, to relate the expansion coefficients to the actual field values, the Yee cell is divided into eight subcells in such a way that the original field node on the Yee cell is surrounded by the eight subcells. We call "subcell" an elementary cubic volume that surrounds a point (node) at which a discrete field component is defined in 3-D space. The example of an E_x node is shown in Fig. 2. The subcells are named lll, llu, lul, and so on, corresponding to the lower (l) or upper (u) position with respect to the Yee's field node along the x-, y-, and z-axes. The centers of the subcells are field sampling points of the new multiresolution grid. We call the center of the subcells "sub node." As one can deduce from Fig. 2, each subcell on the multiresolution grid comprises three electric and three magnetic field components. The number of degrees of freedom for the multiresolution technique is eight times that of the traditional FDTD method having the same Yee grid size. This means that for the same number of degrees of freedom, the multiresolution technique

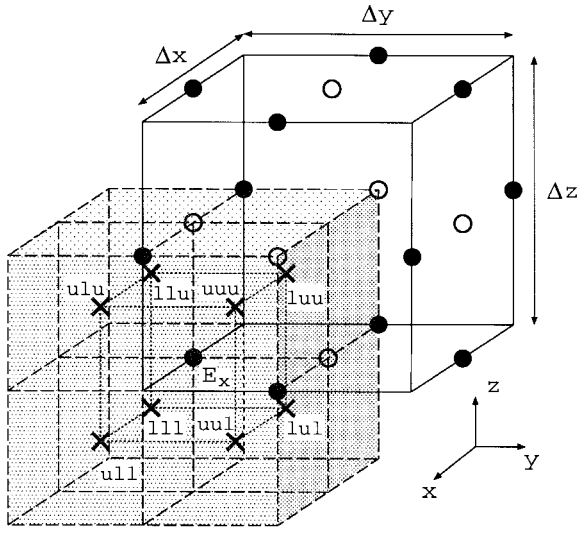

Fig. 2. Eight E_x-subcells (dashed lines) surround a standard FDTD node of E_x on the Yee cell (solid lines). Circles (∘) and black dots (•) represent the magnetic and electric field components defined on the Yee cell, respectively. The centers of the subcells represented by crosses (×) are the field sampling points for the multiresolution grid.

allows twice as coarse grid as the FDTD method.

The following eight rectangular-pulse functions are considered to be a set of 3-D orthogonal basis functions that represent individual subcells:

$$\begin{cases} l_i(x)\,l_j(y)\,l_k(z) \\ l_i(x)\,l_j(y)\,u_k(z) \\ l_i(x)\,u_j(y)\,l_k(z) \\ u_i(x)\,l_j(y)\,l_k(z) \\ l_i(x)\,u_j(y)\,u_k(z) \\ u_i(x)\,l_j(y)\,u_k(z) \\ u_i(x)\,u_j(y)\,l_k(z) \\ u_i(x)\,u_j(y)\,u_k(z) \end{cases} \tag{11}$$

where

$$l_m(w) = l\left(\frac{w - m\Delta w}{\Delta w}\right) \tag{12a}$$

$$u_m(w) = u\left(\frac{w - m\Delta w}{\Delta w}\right), \quad \text{for } (w, m) = (x, i), (y, j), (z, k) \tag{12b}$$

with $l(s)$ and $u(s)$ defined by

$$l(s) = \begin{cases} \sqrt{2}, & \text{for } -1/2 < s \le 0 \\ 0, & \text{otherwise} \end{cases} \tag{13a}$$

$$u(s) = \begin{cases} \sqrt{2}, & \text{for } 0 < s \le 1/2 \\ 0, & \text{otherwise.} \end{cases} \tag{13b}$$

In (13), the factor $\sqrt{2}$ is for the orthonormal property of the functions. The 3-D rectangular-pulse basis functions are also shown in Fig. 3 in the case of an E_x node. To satisfy an orthonormal property of the 3-D rectangular-pulse basis functions, the magnitudes of the functions are chosen to be $\sqrt{8}$. Then the rectangular-pulse basis coefficients ${}^{x}_{n}E^{opq}_{ijk}$ for $o, p, q = l, u$ can be related to the actual field values ${}^{x}_{n}\hat{E}^{opq}_{ijk}$

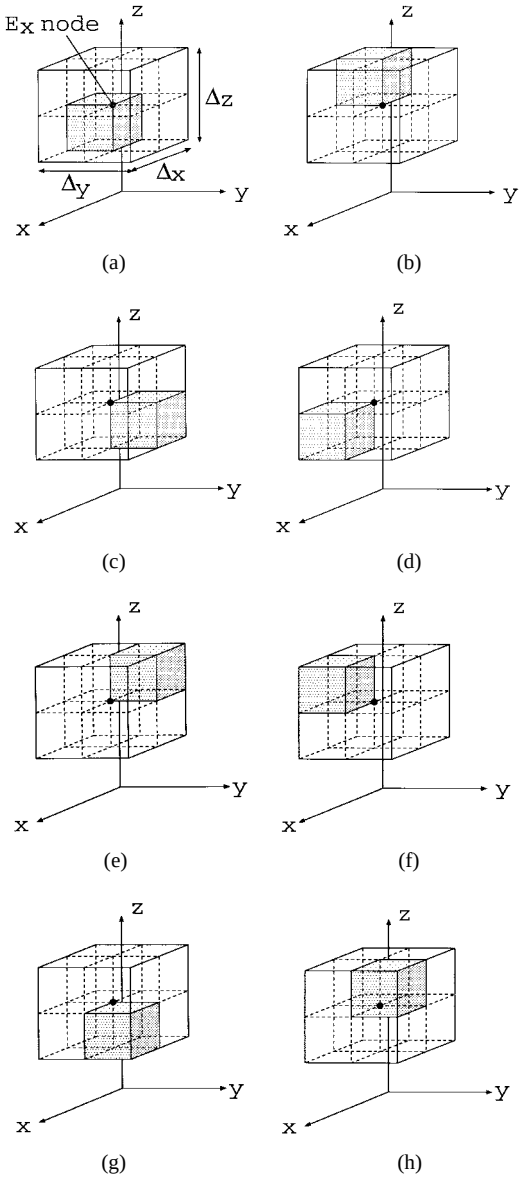

Fig. 3. 3-D rectangular-pulse basis functions for an E_x node. Hatched regions represent $+\sqrt{8}$ and unhatched regions represent zero. Each function represents an individual subcell.

at sampling points in subcells (opq) as

$$\begin{bmatrix} {}^{x}_{n}\hat{E}^{lll}_{ijk} \\ {}^{x}_{n}\hat{E}^{llu}_{ijk} \\ {}^{x}_{n}\hat{E}^{lul}_{ijk} \\ {}^{x}_{n}\hat{E}^{ull}_{ijk} \\ {}^{x}_{n}\hat{E}^{luu}_{ijk} \\ {}^{x}_{n}\hat{E}^{ulu}_{ijk} \\ {}^{x}_{n}\hat{E}^{uul}_{ijk} \\ {}^{x}_{n}\hat{E}^{uuu}_{ijk} \end{bmatrix} = \sqrt{8} \begin{bmatrix} {}^{x}_{n}E^{lll}_{ijk} \\ {}^{x}_{n}E^{llu}_{ijk} \\ {}^{x}_{n}E^{lul}_{ijk} \\ {}^{x}_{n}E^{ull}_{ijk} \\ {}^{x}_{n}E^{luu}_{ijk} \\ {}^{x}_{n}E^{ulu}_{ijk} \\ {}^{x}_{n}E^{uul}_{ijk} \\ {}^{x}_{n}E^{uuu}_{ijk} \end{bmatrix}. \tag{14}$$

Thus, the rectangular-pulse basis coefficients ${}^{x}_{n}E^{opq}_{ijk}$ for $o, p, q = l, u$ can be calculated from the 3-D Haar basis

coefficients ${}^{x}_{n}E^{\zeta\eta\xi}_{ijk}$ for $\zeta, \eta, \xi = \phi, \psi$ as

$$\begin{bmatrix} {}^{x}_{n}E^{lll}_{ijk} \\ {}^{x}_{n}E^{llu}_{ijk} \\ {}^{x}_{n}E^{lul}_{ijk} \\ {}^{x}_{n}E^{ull}_{ijk} \\ {}^{x}_{n}E^{luu}_{ijk} \\ {}^{x}_{n}E^{ulu}_{ijk} \\ {}^{x}_{n}E^{uul}_{ijk} \\ {}^{x}_{n}E^{uuu}_{ijk} \end{bmatrix} = \mathbf{A} \begin{bmatrix} {}^{x}_{n}E^{\phi\phi\phi}_{ijk} \\ {}^{x}_{n}E^{\phi\phi\psi}_{ijk} \\ {}^{x}_{n}E^{\phi\psi\phi}_{ijk} \\ {}^{x}_{n}E^{\psi\phi\phi}_{ijk} \\ {}^{x}_{n}E^{\phi\psi\psi}_{ijk} \\ {}^{x}_{n}E^{\psi\phi\psi}_{ijk} \\ {}^{x}_{n}E^{\psi\psi\phi}_{ijk} \\ {}^{x}_{n}E^{\psi\psi\psi}_{ijk} \end{bmatrix} \tag{15}$$

where

$$\mathbf{A} = \frac{1}{\sqrt{8}} \begin{bmatrix} +1 & +1 & +1 & +1 & +1 & +1 & +1 & +1 \\ +1 & -1 & +1 & +1 & -1 & -1 & +1 & -1 \\ +1 & +1 & -1 & +1 & -1 & +1 & -1 & -1 \\ +1 & +1 & +1 & -1 & +1 & -1 & -1 & -1 \\ +1 & -1 & -1 & +1 & +1 & -1 & -1 & +1 \\ +1 & -1 & +1 & -1 & -1 & +1 & -1 & +1 \\ +1 & +1 & -1 & -1 & -1 & -1 & +1 & +1 \\ +1 & -1 & -1 & -1 & +1 & +1 & +1 & -1 \end{bmatrix} \tag{16}$$

which is a basis transformation matrix between the 3-D Haar basis functions and the rectangular-pulse basis functions.

Matrix $\mathbf{A}$ has the orthogonality property $\mathbf{A}^{\dagger}\mathbf{A} = \mathbf{A}\mathbf{A}^{\dagger} = \mathbf{I}$ (or $\mathbf{A}^{-1} = \mathbf{A}^{\dagger}$), where $\mathbf{A}^{\dagger}$ denotes the transpose matrix and $\mathbf{I}$ the identity matrix. Furthermore, it is symmetric: $\mathbf{A}^{\dagger} = \mathbf{A}$. Therefore, it has the important property

$$\mathbf{A}^{-1} = \mathbf{A} \tag{17}$$

which allows a simple conversion between the expansion coefficients of the rectangular-pulse basis functions and the Haar basis functions as

$$\begin{bmatrix} {}^{w}_{n}E^{\phi\phi\phi}_{ijk} \\ {}^{w}_{n}E^{\phi\phi\psi}_{ijk} \\ {}^{w}_{n}E^{\phi\psi\phi}_{ijk} \\ {}^{w}_{n}E^{\psi\phi\phi}_{ijk} \\ {}^{w}_{n}E^{\phi\psi\psi}_{ijk} \\ {}^{w}_{n}E^{\psi\phi\psi}_{ijk} \\ {}^{w}_{n}E^{\psi\psi\phi}_{ijk} \\ {}^{w}_{n}E^{\psi\psi\psi}_{ijk} \end{bmatrix} = \mathbf{A} \begin{bmatrix} {}^{w}_{n}E^{lll}_{ijk} \\ {}^{w}_{n}E^{llu}_{ijk} \\ {}^{w}_{n}E^{lul}_{ijk} \\ {}^{w}_{n}E^{ull}_{ijk} \\ {}^{w}_{n}E^{luu}_{ijk} \\ {}^{w}_{n}E^{ulu}_{ijk} \\ {}^{w}_{n}E^{uul}_{ijk} \\ {}^{w}_{n}E^{uuu}_{ijk} \end{bmatrix}, \qquad \text{for } w = x, y, z. \tag{18}$$

C. Perfect Electric Conductor (PEC) Boundary Conditions

1) One-Dimensional Case: The implementation of PEC boundary conditions is first described for the one-dimensional case. As discussed in [9], the basis functions do not couple at the inner computational nodes, but only at the boundary and the excitation nodes. Therefore, the PEC condition is implemented by combining scaling and wavelet functions at the boundaries such that the tangential electric field at the boundaries becomes zero. At the same time, the electric field in the subcell situated half a cell size away from the boundary must be found by interpolation so that the tangential electric field varies smoothly in front of the boundary. Fig. 4 shows a one-dimensional PEC boundary placed at $x = x^{l}_{0} = 0$. In contrast to the condition presented in [10], the boundary is located at the position that is shifted by $\Delta x/4$ from the center of the basis functions. This saves a subcell at the boundary rather than locating the boundary at the center of the basis functions. Since the tangential electric field at the boundary is zero, the first equation is given by

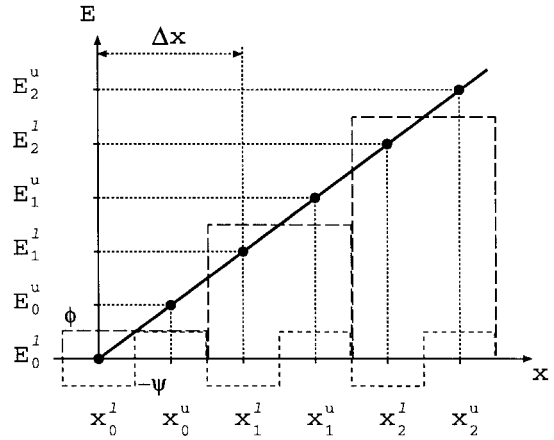

Fig. 4. Schematic diagram of tangential electric fields near a one-dimensional PEC boundary at $x = x^{l}_{0} = 0$. Long dashed lines (– – –) and short dashed lines (- - -) show Haar scaling (ϕ) and wavelet ($-\psi$) functions, respectively. Closed circles (•) show the sampling points for the proposed multiresolution grid.

$$E^{l}_{0} \equiv \frac{1}{\sqrt{2}}\left(E^{\phi}_{0} + E^{\psi}_{0}\right) = 0. \tag{19}$$

The tangential electric field at $x = x^{u}_{0}$ is expanded into a Taylor series with respect to $x = x^{l}_{1}$ as

$$E(x^{u}_{0}) = E(x^{l}_{1}) + (x^{u}_{0} - x^{l}_{1})E'(x^{l}_{1}) + \cdots \tag{20}$$

and the backward-difference approximation is used for the first derivative

$$E'(x^{l}_{1}) \approx E(x^{l}_{1})/x^{l}_{1} \tag{21}$$

then the second equation is given at $x = x^{u}_{0}$ by

$$\begin{aligned} E^{u}_{0} &\equiv \frac{1}{\sqrt{2}}\left(E^{\phi}_{0} - E^{\psi}_{0}\right) \\ &= \frac{x^{u}_{0}}{x^{l}_{1}}E^{l}_{1} \\ &= \frac{x^{u}_{0}}{x^{l}_{1}} \cdot \frac{1}{\sqrt{2}}\left(E^{\phi}_{1} + E^{\psi}_{1}\right). \end{aligned} \tag{22}$$

Solving (19) and (22) in terms of the Haar basis coefficients E^{ϕ}_{0} and E^{ψ}_{0} leads to the boundary condition at $x = 0$

$$E^{\phi}_{0} = -E^{\psi}_{0} = \frac{x^{u}_{0}}{2x^{l}_{1}}\left(E^{\phi}_{1} + E^{\psi}_{1}\right). \tag{23}$$

Similarly, by using a forward-difference approximation, the PEC condition for the other side of the boundary at $x = x_M$ can be obtained as

$$E^{\phi}_{M} = E^{\psi}_{M} = \frac{x^{u}_{M} - x^{l}_{M}}{2(x^{u}_{M} - x^{u}_{M-1})}\left(E^{\phi}_{M-1} - E^{\psi}_{M-1}\right). \tag{24}$$

The PEC conditions (23) and (24) lead to a slightly distorted field distribution, which can be improved by using Lagrange interpolation instead of the forward- or the backward-difference approximation. Since the tangential electric field near the boundary is considered to be an odd function about the boundary, a third-order interpolation polynomial is obtained by using only two reference points as known field values. This is the same requirement as is used in the central-difference approximation for the first derivative in the Taylor series of (20).

In the case of a PEC boundary at $x = 0$, the electric field E_0^u at $x = x_0^u$ is interpolated from those at $x = x_1^l$ and x_2^l. The third-order Lagrange coefficient polynomials are given by

$$L_1(x) = \frac{x\{(x)^2 - (x_2^l)^2\}}{x_1^l\{(x_1^l)^2 - (x_2^l)^2\}} \tag{25a}$$

$$L_2(x) = \frac{x\{(x)^2 - (x_1^l)^2\}}{x_2^l\{(x_2^l)^2 - (x_1^l)^2\}}. \tag{25b}$$

Thus, E_0^u is given by Lagrange interpolation as

$$\begin{aligned} E_0^u &\equiv \frac{1}{\sqrt{2}}\left(E_0^\phi - E_0^\psi\right) \\ &= L_1(x_0^u)E_1^l + L_2(x_0^u)E_2^l \\ &= L_1(x_0^u)\cdot\frac{1}{\sqrt{2}}\left(E_1^\phi + E_1^\psi\right) + L_2(x_0^u)\cdot\frac{1}{\sqrt{2}}\left(E_2^\phi + E_2^\psi\right). \end{aligned} \tag{26}$$

Solving (19) and (26) in terms of E_0^ϕ and E_0^ψ leads to an improved PEC boundary condition at $x = 0$

$$\begin{aligned} E_0^\phi &= -E_0^\psi \\ &= \tfrac{1}{2}\left\{L_1(x_0^u)\left(E_1^\phi + E_1^\psi\right) + L_2(x_0^u)\left(E_2^\phi + E_2^\psi\right)\right\}. \end{aligned} \tag{27}$$

Similarly, the PEC boundary condition at $x = x_M$ can be obtained as

$$\begin{aligned} E_M^\phi &= E_M^\psi \\ &= \frac{1}{2}\left\{L_{M-1}(x_M^l)\left(E_{M-1}^\phi - E_{M-1}^\psi\right)\right. \\ &\qquad \left. + L_{M-2}(x_M^l)\left(E_{M-2}^\phi - E_{M-2}^\psi\right)\right\} \end{aligned} \tag{28}$$

where the coefficient polynomials are given by

$$L_{M-1}(x) = \frac{x\{(x)^2 - (x_{M-2}^u)^2\}}{x_{M-1}^u\{(x_{M-1}^u)^2 - (x_{M-2}^u)^2\}} \tag{29a}$$

$$L_{M-2}(x) = \frac{x\{(x)^2 - (x_{M-1}^u)^2\}}{x_{M-2}^u\{(x_{M-2}^u)^2 - (x_{M-1}^u)^2\}}. \tag{29b}$$

2) 3-D Case: To implement the PEC condition that is perpendicular to the x-axis in three space dimensions, the three-dimensional Haar basis functions are divided into four pairs in such a way that the functions having the same variation in y- and z-directions form a pair as follows:

$$\begin{cases} [\phi_i(x)\,\phi_j(y)\,\phi_k(z),\ \psi_i(x)\,\phi_j(y)\,\phi_k(z)] \\ [\phi_i(x)\,\phi_j(y)\,\psi_k(z),\ \psi_i(x)\,\phi_j(y)\,\psi_k(z)] \\ [\phi_i(x)\,\psi_j(y)\,\phi_k(z),\ \psi_i(x)\,\psi_j(y)\,\phi_k(z)] \\ [\phi_i(x)\,\psi_j(y)\,\psi_k(z),\ \psi_i(x)\,\psi_j(y)\,\psi_k(z)] \end{cases}. \tag{30}$$

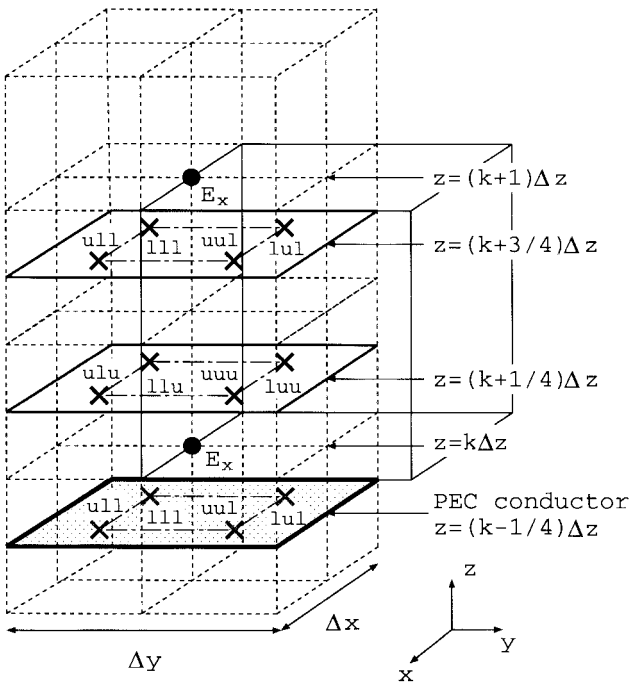

Fig. 5. Location of a PEC boundary parallel to the xy-plane (thick solid line). A unit Yee cell is marked by thin solid lines.

Then, the tangential electric fields E_y and E_z at the boundary are set to zero as described for the one-dimensional case.

At $x = 0$ $(i = 0)$, the 3-D PEC conditions are given by

$$\begin{aligned} {}_n^w E_{0jk}^{\phi\eta\xi} &= -{}_n^w E_{0jk}^{\psi\eta\xi} \\ &= \frac{x_0^u}{2x_1^l}\left({}_n^w E_{1jk}^{\phi\eta\xi} + {}_n^w E_{1jk}^{\psi\eta\xi}\right), \\ &\qquad \text{for } w = y,\ z \text{ and } \eta,\ \xi = \phi,\ \psi. \end{aligned} \tag{31}$$

For the other side of the boundary at $x = x_M$ $(i = M)$, with the same pairs, the conditions are given by

$$\begin{aligned} {}_n^w E_{Mjk}^{\phi\eta\xi} &= {}_n^w E_{Mjk}^{\psi\eta\xi} \\ &= \frac{x_M^u - x_M^l}{2(x_M^u - x_{M-1}^u)}\left({}_n^w E_{M-1\ jk}^{\phi\eta\xi} - {}_n^w E_{M-1\ jk}^{\psi\eta\xi}\right), \\ &\qquad \text{for } w = y,\ z \text{ and } \eta,\ \xi = \phi,\ \psi. \end{aligned} \tag{32}$$

The boundary conditions for the other directions can be derived similarly. Equations (31) and (32) are computed for all the pairs of the basis functions. The implementation of the Lagrange interpolation technique is also available in the three-dimensional case.

To give a clear view of the implementation of the PEC condition, the implementation of the perfect electric planer conductor is described in the following. Referring to the notations in Fig. 2, we assume, as shown in Fig. 5, that the PEC boundary is parallel to the xy-plane and cuts across the center of the four subcells lll, lul, ull, and uul at $z = (k - 1/4)\Delta z$. Then the field values in the upper subcells llu, luu, ulu and uuu at $z = (k + 1/4)\Delta z$ are determined by interpolation between the fields on the conductor, which are zero, and the fields in the subcells lll, lul, ull, and uul at

TABLE I
COMPARISON OF THE NUMBER OF DEGREES OF FREEDOM (NDF), THE NORMALIZED DOMINANT RESONANT FREQUENCY, AND THE COMPUTATIONAL TIME

No. of Yee cells	No. of time steps	proposed technique			conventional FDTD		
		NDF	norm. freq.	CPU time* (sec)	NDF	norm. freq.	CPU time* (sec)
4×4×2	1500	1536	.9908	3.3	192	.9805	2.8
8×8×4	3000	12288	.9966	12.9	1536	.9952	6.4
16×16×8	6000	98304	.9990	193.2	12288	.9988	30.4
32×32×16	12000	—	—	—	98304	.9997	456.8

*CPU time on HP9000/C160 workstation

$z = (k + 3/4)\Delta z$. By taking simple averaging, we have

$$\begin{bmatrix} {}^{w}_{n}E^{lll}_{ijk} \\ {}^{w}_{n}E^{llu}_{ijk} \\ {}^{w}_{n}E^{lul}_{ijk} \\ {}^{w}_{n}E^{ull}_{ijk} \\ {}^{w}_{n}E^{luu}_{ijk} \\ {}^{w}_{n}E^{ulu}_{ijk} \\ {}^{w}_{n}E^{uul}_{ijk} \\ {}^{w}_{n}E^{uuu}_{ijk} \end{bmatrix} = \frac{1}{2} \begin{bmatrix} 0 \\ {}^{w}_{n}E^{lll}_{ijk+1} \\ 0 \\ 0 \\ {}^{w}_{n}E^{lul}_{ijk+1} \\ {}^{w}_{n}E^{ull}_{ijk+1} \\ 0 \\ {}^{w}_{n}E^{uul}_{ijk+1} \end{bmatrix}, \qquad \text{for } w = x, y. \tag{33}$$

Hence, the 3-D Haar basis coefficients for E_x and E_y components can be calculated using the basis transformation matrix $\mathbf{A}$ as (18).

D. Absorbing Boundary Conditions

Mur's first-order ABC has been implemented in this paper. The ABC's in the traditional FDTD method can be implemented independently for each coefficient associated with the three-dimensional Haar basis function. The outgoing wave associated with each basis function is absorbed independently by each corresponding ABC. Therefore, the implementation of ABC's in the new multiresolution technique is similar to the traditional FDTD method.

III. VALIDATION

The accuracy and the computational time of the new multiresolution technique were first investigated by analyzing a rectangular cavity with normalized dimensions of $0.5\sqrt{2} \times 0.5\sqrt{2} \times 0.2$ for a TE_{110} mode having a normalized dominant resonant frequency of 1.0. (The normalized speed of light was assumed to be unity.) The number of time steps was determined so that the computed resonant frequencies converge. The excitation occurred at the center of the cavity with a raised-cosine-modulated sine wave pulse, which had a normalized center frequency of approximately 1.0. The time discretization interval was chosen to be 0.8 times the Courant limit for both methods. By selecting a time discretization interval twice that of the traditional FDTD method, the computational time was approximately half that of the traditional FDTD method for the same number of degrees of freedom. The results are summarized in Table I. Both the accuracy and the computational time of the proposed technique lie between those of a conventional FDTD having the same number of degrees of freedom and one having an eighth the number of degrees of freedom.

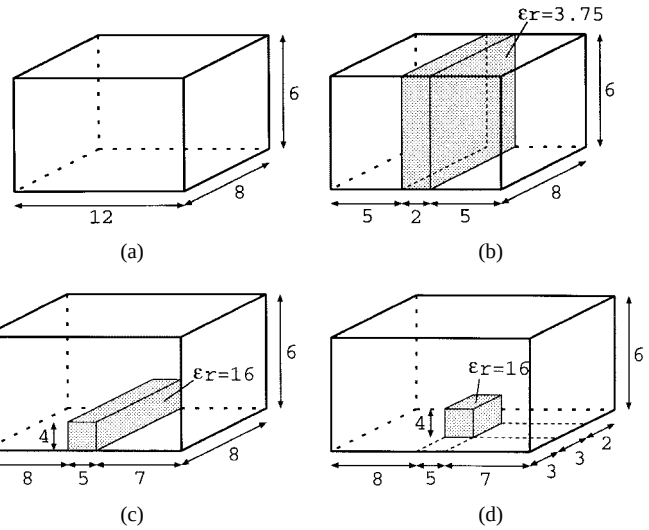

Fig. 6. Three-dimensional rectangular cavities analyzed in this study.

TABLE II
NORMALIZED DOMINANT RESONANT FREQUENCIES OF RECTANGULAR CAVITIES

cavity	proposed technique (*i*) (Yee cells)	conventional FDTD (*ii*) (Yee cells)	% difference $\frac{(i)-(ii)}{(ii)}$	analytical
(a)	0.07542 (6×4×3)	0.07486 (12×8×6)	+0.75	0.07511
(b)	0.05302 (5×4×3)*	0.05228 (12×8×6)	+1.42	0.05221
(c)	0.02764 (10×4×3)*	0.02661 (20×8×6)	+3.87	--
(d)	0.03834 (10×5×3)*	0.03908 (20×8×6)	−1.89	—

*nonuniform grids

Four rectangular cavities loaded with inhomogeneous dielectric materials described in [15] were then analyzed with the proposed technique. The dominant resonant frequencies were compared with analytical values (when available) and those obtained with the conventional FDTD method. The geometries of the four cavities are shown in Fig. 6 and the results are summarized in Table II. The number of cells in the proposed technique was approximately an eighth of the number of FDTD cells so that the number of degrees of freedom was approximately the same for both methods. To discretize the geometry of the dielectric materials accurately, nonuniform grids were incorporated in the cases (b)–(d). In the case of the homogeneous dielectric cavity (a), the results obtained with both methods agreed within ±1% for the same number of degrees of freedom.

In this new multiresolution technique, the inhomogeneous dielectric interfaces have an anisotropic property due to the approximate treatment of the interfaces. Suppose the dielectric interface is now located at the interface of the Yee cells. Since each unit Yee cell is divided into eight subcells, and each subcell includes three electric and three magnetic field

TABLE III
HIGHER ORDER RESONANT FREQUENCIES IN A CAVITY ANALYZED WITH THE PROPOSED TECHNIQUE

mode	theoretical	numerical	% error
TE_{110}	1.0	0.9992	-0.08
TE_{130}, TE_{310}	$\sqrt{5}$	2.2156	-0.92
TE_{330}	3.0	2.9760	-0.80
TE_{150}, TE_{510}	$\sqrt{13}$	3.5054	-2.78

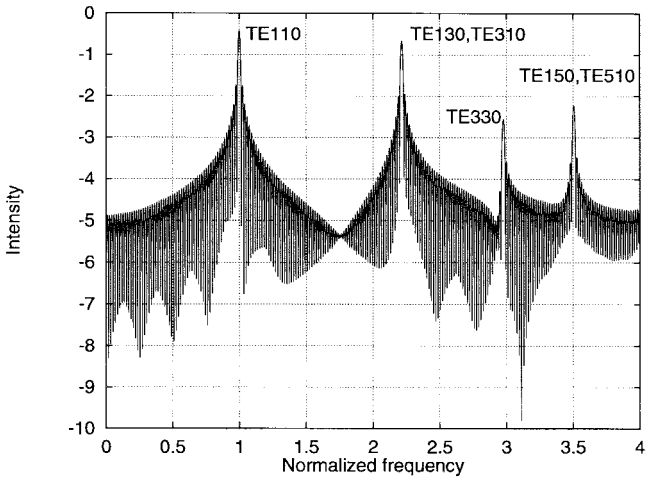

Fig. 7. Frequency spectrum of the higher order mode in a cavity analyzed with the proposed technique.

sampling points collocated at the center of the subcell, the subcell located at each side of the interface includes two tangential and one normal electric field component to the interface. Then the tangential electric fields sense an average dielectric constant between each side of the interface, where as the normal electric field senses a dielectric constant specified at each side. Therefore, the dielectric constants become an isotropic at a layer on each side of the interface.

This approximate property generates instability problems when analyzing structures with inhomogeneous dielectric materials, although it is stable for structures with homogeneous dielectric materials. The dielectric interface can be accurately modeled by introducing the D–H formulation of Maxwell's equations which will be discussed later. It is also noted that, in the analysis of open boundary structures such as microstrip components, the approximate scheme is stable enough for time signals to converge.

Although the analyses so far incorporate PEC boundaries modeled with simple forward- or backward-difference approximations, the PEC boundaries modeled with Lagrange interpolation improve the field distributions more smoothly. The higher order resonances in a cavity with normalized dimensions $1/\sqrt{2} \times 1/\sqrt{2} \times 1/\sqrt{2}$ were analyzed in the following. The cavity was discretized with $16 \times 16 \times 16$ Yee cells and excited with a sine-modulated raised-cosine-wave pulse, which had a normalized center frequency of 3.0. The calculation was done for 3000 time steps with Δt equals 0.8 times the Courant limit, which is $\Delta t = 0.0198$. The analytical and computed normalized resonant frequencies are compared in Table III. The frequency spectrum and the field distribution at time step of 1200 are shown in Figs. 7 and 8, respectively.

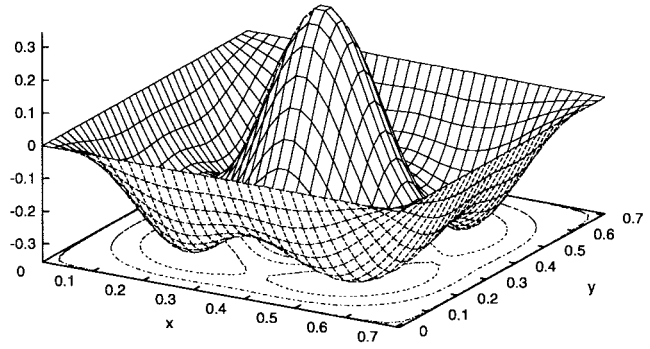

Fig. 8. Field distribution at time step of 1200 for the TE_{ij0} $(i, j = 1, 3, 5, \cdots)$ higher order mode analysis.

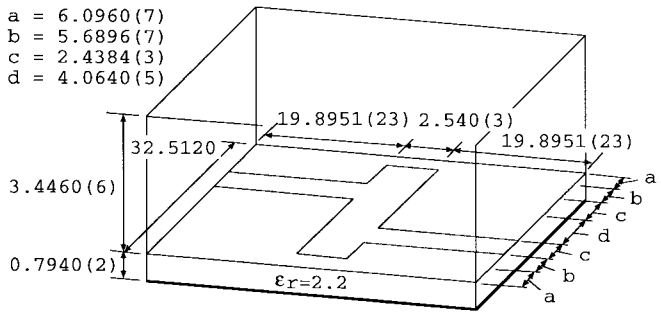

Fig. 9. Microstrip low-pass filter configuration under investigation. The dimensions are in millimeters, and the numbers in parentheses show the numbers of Yee cells.

IV. ANALYSIS OF MICROSTRIP PLANAR CIRCUITS

Two configurations, a low-pass filter and a spiral inductor, were analyzed with both the proposed technique and the conventional FDTD method. Mur's first-order ABC was implemented to extract their S-parameters. The results were compared to demonstrate the capability of the new technique for analyzing realistic microwave components. The computation was done on a HP9000/C160 workstation.

A. Microstrip Low-Pass Filter

The proposed technique was applied to the analysis of the microstrip low-pass filter shown in Fig. 9 [16]. The Yee grid lines used in the analysis are shown in the figure together with the geometrical dimensions. Nonuniform grids were incorporated only in the proposed technique to accurately discretize the geometry of the circuit.

The structure was also analyzed with the conventional FDTD method using the spatial discretization described in [16]. The time discretization was chosen to be 0.98 times the Courant limit for both methods. The excitation pulse was a raised-cosine pulse having a duration time of 66.3 ps. The center frequency of the excitation pulse was approximately 15 GHz. The analysis conditions for both methods are listed in Table IV. The discretization was such that the number of degrees of freedom was approximately the same for both methods. Because, in the proposed technique, the minimum grid dimension was approximately twice that of the conventional FDTD method, the time discretization interval could be

TABLE IV
ANALYSIS CONDITIONS FOR THE MICROSTRIP LOW-PASS FILTER

	proposed technique	conventional FDTD
No. of Yee cells	49×39×8 (non-uniform)	100×80×16 (uniform)
Δt	0.67694 ps	0.43325 ps
No. of time steps	2560	4000
computational time	11m 32.5s	20m 45.5s

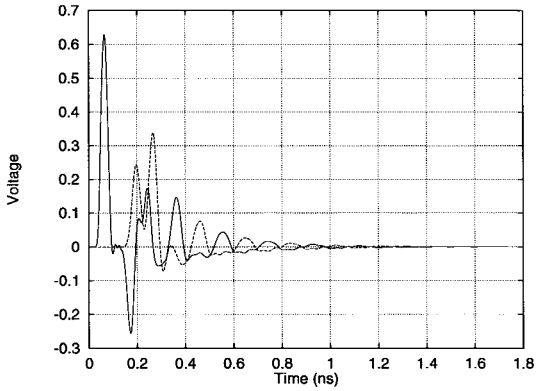

Fig. 10. Time signals of the low-pass filter computed with the proposed technique. The maximum time step is 2560. —: input port, - - -: output port.

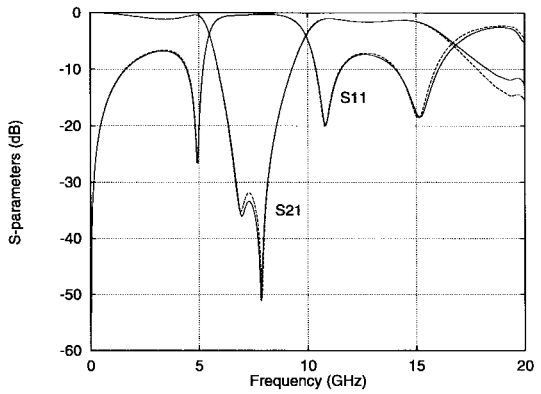

Fig. 11. Computed S-parameters of the low-pass filter. —: proposed method, - - -: conventional FDTD method.

approximately twice that of the conventional FDTD method. This allowed the calculation time for the proposed method approximately half that of the conventional FDTD method.

The resulting time signals and the S-parameters are shown in Figs. 10 and 11, respectively. The S-parameters indicate good agreement between both methods, except for slight deviations in the high-frequency range over 16 GHz and in the small signal range below -30 dB. The time signals were taken until 2560 time steps for the new multiresolution technique. The extensive numerical analysis showed that the scheme was stable at 10^5 time steps.

The snapshots of the E_z field immediately below the microstrip conductors at time 346.6 ps are plotted in Fig. 12. In the proposed technique, a ripple was observed on the excitation side of the filter, while in the conventional FDTD method, the waveform was smooth. This ripple was due to the interaction between the incident pulse and the signal reflected from the filter structure, therefore, it did not appear after passing the filter. This ripple also had a static feature; it did not change in time. Therefore, it did not affect the computed S-parameters either. In case the smooth field distributions are desired, one can obtain them from the scaling function coefficients by using some interpolation technique.

B. Spiral Inductor

A two-turn spiral inductor shown in Fig. 13 was investigated. The relative permittivity and the dimension of the substrate were 9.6 and 50 mm $\times$ 50 mm, respectively. The dimension of the inductor was 18 mm $\times$ 18 mm. The cutoff frequency of the inductor was around 2.5 GHz. Uniform grids were incorporated to discretize the structure for both methods except for the z-direction in the upper air region in the multiresolution technique. The discretization conditions and the calculation time are listed in Table V. The time discretization is also 0.98 times the Courant limit. The excitation pulse was a raised-cosine pulse having the duration time of 333 ps. The center frequency of the excitation pulse was approximately 3 GHz.

The time signals obtained with the proposed technique are shown in Fig. 14. The time signals decayed more slowly than those in the low-pass filter analyzed in the previous subsection due to the long line length of the spiral inductor and the larger permittivity of the substrate. The extensive computation showed that the proposed technique was stable up to the time step of 10^5. The S-parameters of the inductor are shown in Fig. 15 for both methods. It should be mentioned that due to the large permittivity of the substrate, a large reflection from the ABC was observed for both methods. Thus, in calculating the reference data at the input port, computation was terminated by the time the reflection from the ABC reached the input port. This treatment made the energy of the reference signal smaller than that of the signals from the inductor and resulted in the magnitude of the S-parameters being larger than 0 dB. In order to eliminate this discrepancy, the S-parameters in Fig. 15 were offset by about -0.3 dB. The resulting S-parameters demonstrate good agreement of both methods except for the small signal region below -10 dB.

The snapshots of an E_z field immediately below the microstrip conductors at time 1.72 ns are plotted in Fig. 16. In the proposed technique, a ripple was observed on the excitation side of the inductor as well as in the low-pass filter analysis.

V. EXACT FORMULATION FOR THREE-DIMENSIONAL INHOMOGENEOUS DIELECTRIC STRUCTURES

The exact formulation for three-dimensional inhomogeneous dielectric structures is obtained by discretizing Maxwell's equations (1a) and

$$\nabla \times \mathbf{H} = \frac{\partial \mathbf{D}}{\partial t} + \mathbf{J} \tag{34}$$

and the material equation

$$\mathbf{D} = \epsilon \mathbf{E} \tag{35}$$

where the conductivity of the material is assumed to be zero.

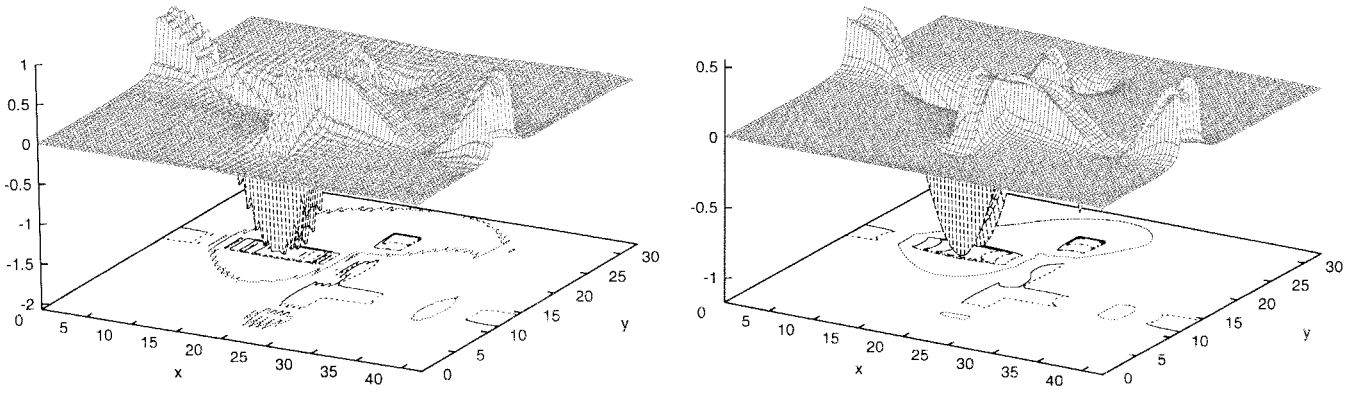

Fig. 12. The snapshots of an E_z field distribution at time 346.6 ps in the low-pass filter immediately below the conductors.

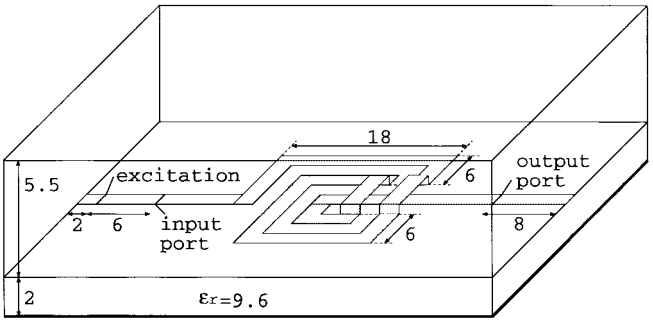

Fig. 13. Spiral inductor configuration under investigation. The dimensions are in millimeters. The line widths and spacings are all 2.0 mm. The height and the span of the air bridges are 1.0 and 6.0 mm, respectively.

TABLE V
ANALYSIS CONDITIONS FOR THE SPIRAL INDUCTOR

	proposed technique	conventional FDTD
Yee cells	62×42×13 (non-uniform)	100×68×26 (uniform)
Δx, Δy	0.8 mm	0.5 mm
Δz	0.5 mm, 0.4524 mm	0.25 mm
Δt	0.37274 ps	0.21535 ps
time steps	23110	40000
CPU time	3h 38m 2.9s	5h 4m 32.5s

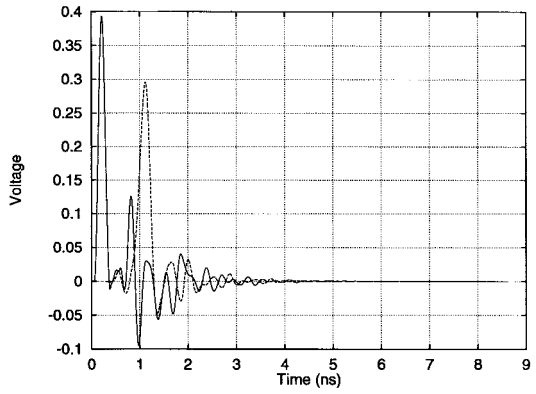

Fig. 14. Time signals of the spiral inductor computed with the proposed technique. The maximum time step is 23 110. —: input port, - - -: output port.

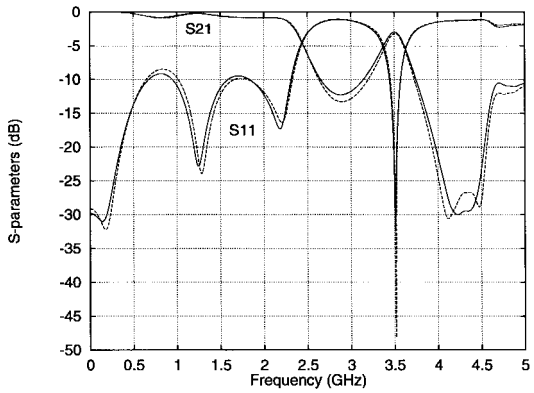

Fig. 15. Computed S-parameters of the spiral inductor. —: proposed method, - - -: conventional FDTD method.

The electric flux density, D_x for example, is expanded using the 3-D Haar basis functions (2) as

$$
\begin{aligned}
D_x(\vec{r},\, t) = \sum_{i=0}^{I}\sum_{j=0}^{J}\sum_{k=0}^{K}\sum_{n=0}^{N} h_n(t) \\
\cdot \Big\{ {}^{x}_{n}D^{\phi\phi\phi}_{i+1/2,\,j,\,k}\,\phi_{i+1/2}(x)\,\phi_j(y)\,\phi_k(z) \\
+ {}^{x}_{n}D^{\phi\phi\psi}_{i+1/2,\,j,\,k}\,\phi_{i+1/2}(x)\,\phi_j(y)\,\psi_k(z) \\
+ {}^{x}_{n}D^{\phi\psi\phi}_{i+1/2,\,j,\,k}\,\phi_{i+1/2}(x)\,\psi_j(y)\,\phi_k(z) \\
+ {}^{x}_{n}D^{\psi\phi\phi}_{i+1/2,\,j,\,k}\,\psi_{i+1/2}(x)\,\phi_j(y)\,\phi_k(z) \\
+ {}^{x}_{n}D^{\phi\psi\psi}_{i+1/2,\,j,\,k}\,\phi_{i+1/2}(x)\,\psi_j(y)\,\psi_k(z) \\
+ {}^{x}_{n}D^{\psi\phi\psi}_{i+1/2,\,j,\,k}\,\psi_{i+1/2}(x)\,\phi_j(y)\,\psi_k(z) \\
+ {}^{x}_{n}D^{\psi\psi\phi}_{i+1/2,\,j,\,k}\,\psi_{i+1/2}(x)\,\psi_j(y)\,\phi_k(z) \\
+ {}^{x}_{n}D^{\psi\psi\psi}_{i+1/2,\,j,\,k}\,\psi_{i+1/2}(x)\,\psi_j(y)\,\psi_k(z) \Big\} \qquad (36)
\end{aligned}
$$

where the notations are defined as in (6) and (7).

Then, the similar procedure used for (8) and (9) leads to the time iterative difference equations with the weighted voltage across the E-node ${}^{w}_{n}W^{\zeta\eta\xi}_{i,\,j,\,k} \equiv {}^{w}_{n}D^{\zeta\eta\xi}_{i,\,j,\,k}\,\Delta w$ for $w = x,\, y,\, z$

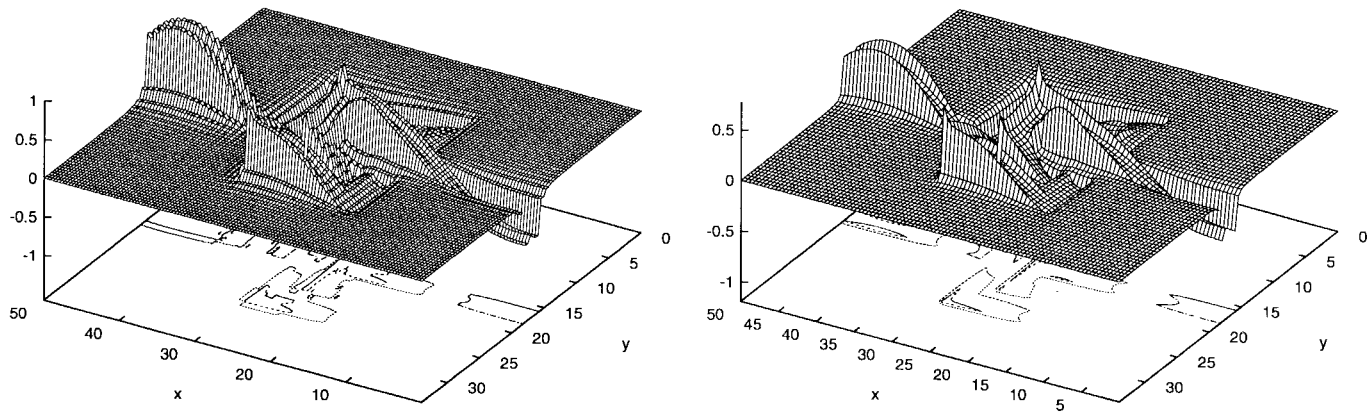

Fig. 16. The snapshots of an E_z field distribution at time 1.72 ns of the spiral inductor immediately below the microstrip conductors.

and $\zeta, \eta, \xi = \phi, \psi$ as

$$ {}^{x}_{h}I^{\zeta\eta\xi}_{0h\bar{h}} = {}^{x}_{\bar{h}}I^{\zeta\eta\xi}_{0h\bar{h}} - \frac{\Delta t}{\mu}\left[\frac{\Delta x}{\Delta y\,\Delta z}\right]_{0hh} \cdot \left\{ {}^{z}_{0}V^{\zeta\eta\xi}_{01\bar{h}} - {}^{z}_{0}V^{\zeta\eta\xi}_{00\bar{h}} - ({}^{y}_{0}V^{\zeta\eta\xi}_{0h1} - {}^{y}_{0}V^{\zeta\eta\xi}_{0h0}) \right\} \quad (37a) $$

$$ {}^{y}_{h}I^{\zeta\eta\xi}_{h0\bar{h}} = {}^{y}_{\bar{h}}I^{\zeta\eta\xi}_{h0\bar{h}} - \frac{\Delta t}{\mu}\left[\frac{\Delta y}{\Delta z\,\Delta x}\right]_{h0h} \cdot \left\{ {}^{x}_{0}V^{\zeta\eta\xi}_{h01} - {}^{x}_{0}V^{\zeta\eta\xi}_{h00} - ({}^{z}_{0}V^{\zeta\eta\xi}_{10\bar{h}} - {}^{z}_{0}V^{\zeta\eta\xi}_{00\bar{h}}) \right\} \quad (37b) $$

$$ {}^{z}_{h}I^{\zeta\eta\xi}_{hh0} = {}^{z}_{\bar{h}}I^{\zeta\eta\xi}_{hh0} - \frac{\Delta t}{\mu}\left[\frac{\Delta z}{\Delta x\,\Delta y}\right]_{h00} \cdot \left\{ {}^{y}_{0}V^{\zeta\eta\xi}_{1h0} - {}^{y}_{0}V^{\zeta\eta\xi}_{0h0} - ({}^{x}_{0}V^{\zeta\eta\xi}_{h10} - {}^{x}_{0}V^{\zeta\eta\xi}_{h00}) \right\} \quad (37c) $$

and

$$ {}^{x}_{1}W^{\zeta\eta\xi}_{h00} = {}^{x}_{0}W^{\zeta\eta\xi}_{h00} + \Delta t\left[\frac{\Delta x}{\Delta y\,\Delta z}\right]_{h00} \cdot \left\{ {}^{z}_{h}I^{\zeta\eta\xi}_{hh0} - {}^{z}_{\bar{h}}I^{\zeta\eta\xi}_{\bar{h}h0} - ({}^{y}_{h}I^{\zeta\eta\xi}_{h0\bar{h}} - {}^{y}_{\bar{h}}I^{\zeta\eta\xi}_{h0\bar{h}}) - {}^{x}_{h}\hat{I}^{\zeta\eta\xi}_{h00} \right\} \quad (38a) $$

$$ {}^{y}_{1}W^{\zeta\eta\xi}_{0h0} = {}^{y}_{0}W^{\zeta\eta\xi}_{0h0} + \Delta t\left[\frac{\Delta y}{\Delta z\,\Delta x}\right]_{0h0} \cdot \left\{ {}^{x}_{h}I^{\zeta\eta\xi}_{0hh} - {}^{x}_{\bar{h}}I^{\zeta\eta\xi}_{0\bar{h}h} - ({}^{z}_{h}I^{\zeta\eta\xi}_{hh0} - {}^{z}_{\bar{h}}I^{\zeta\eta\xi}_{\bar{h}h0}) - {}^{y}_{h}\hat{I}^{\zeta\eta\xi}_{0h0} \right\} \quad (38b) $$

$$ {}^{z}_{1}W^{\zeta\eta\xi}_{00h} = {}^{z}_{0}W^{\zeta\eta\xi}_{00h} + \Delta t\left[\frac{\Delta z}{\Delta x\,\Delta y}\right]_{00h} \cdot \left\{ {}^{y}_{h}I^{\zeta\eta\xi}_{h0h} - {}^{y}_{\bar{h}}I^{\zeta\eta\xi}_{\bar{h}0h} - ({}^{x}_{h}I^{\zeta\eta\xi}_{0hh} - {}^{x}_{\bar{h}}I^{\zeta\eta\xi}_{0\bar{h}h}) - {}^{z}_{h}\hat{I}^{\zeta\eta\xi}_{00h} \right\}. \quad (38c) $$

The material equation (35) can be also discretized using 3-D Haar scaling and wavelet basis (2) as discussed in [13] in the case of Battle–Lemarie scaling and wavelet basis. However, in the case of 3-D Haar scaling and wavelet basis, it is more simply discretized with using the basis transformation matrix $\mathbf{A}$. For isotropic dielectric materials, the material (35) is written for a rectangular subcell (opq) for $o, p, q = l, u$ in a unit Yee cell as

$$ {}^{w}D^{opq}_{ijk} = \epsilon^{opq}_{ijk}\,{}^{w}E^{opq}_{ijk}, \qquad \text{for } w = x, y, z. \quad (39) $$

This can be rewritten in a matrix form as

$$ [{}^{w}E_{ijk}]_{rec} = [\epsilon^{-1}_{ijk}]_{rec}\,[{}^{w}D_{ijk}]_{rec}, \qquad \text{for } w = x, y, z \quad (40) $$

where

$$ [{}^{w}E_{ijk}]_{rec} = \begin{bmatrix} {}^{w}E^{lll}_{ijk} \\ {}^{w}E^{llu}_{ijk} \\ {}^{w}E^{lul}_{ijk} \\ {}^{w}E^{ull}_{ijk} \\ {}^{w}E^{luu}_{ijk} \\ {}^{w}E^{ulu}_{ijk} \\ {}^{w}E^{uul}_{ijk} \\ {}^{w}E^{uuu}_{ijk} \end{bmatrix} \quad (41) $$

$$ [{}^{w}D_{ijk}]_{rec} = \begin{bmatrix} {}^{w}D^{lll}_{ijk} \\ {}^{w}D^{llu}_{ijk} \\ {}^{w}D^{lul}_{ijk} \\ {}^{w}D^{ull}_{ijk} \\ {}^{w}D^{luu}_{ijk} \\ {}^{w}D^{ulu}_{ijk} \\ {}^{w}D^{uul}_{ijk} \\ {}^{w}D^{uuu}_{ijk} \end{bmatrix} \quad (42) $$

and $\left[\epsilon^{-1}_{ijk}\right]_{rec}$ is shown in (43) at the bottom of the following page. Since the matrix $\mathbf{A}$ is the basis transformation matrix between the rectangular-pulse basis functions and the Haar basis functions, (40) can be transformed into the Haar basis coefficients using relation (17) as

$$ [{}^{w}E_{ijk}]_{\text{Haar}} = \left[\epsilon^{-1}_{ijk}\right]_{\text{Haar}}[{}^{w}D_{ijk}]_{\text{Haar}}, \qquad \text{for } w = x, y, z, \quad (44) $$

where

$$[{}^{w}E_{ijk}]_{\text{Haar}} = \begin{bmatrix} {}^{w}E_{ijk}^{\phi\phi\phi} \\ {}^{w}E_{ijk}^{\phi\phi\psi} \\ {}^{w}E_{ijk}^{\phi\psi\phi} \\ {}^{w}E_{ijk}^{\psi\phi\phi} \\ {}^{w}E_{ijk}^{\phi\psi\psi} \\ {}^{w}E_{ijk}^{\psi\phi\psi} \\ {}^{w}E_{ijk}^{\psi\psi\phi} \\ {}^{w}E_{ijk}^{\psi\psi\psi} \end{bmatrix} \tag{45}$$

$$[{}^{w}D_{ijk}]_{\text{Haar}} = \begin{bmatrix} {}^{w}D_{ijk}^{\phi\phi\phi} \\ {}^{w}D_{ijk}^{\phi\phi\psi} \\ {}^{w}D_{ijk}^{\phi\psi\phi} \\ {}^{w}D_{ijk}^{\psi\phi\phi} \\ {}^{w}D_{ijk}^{\phi\psi\psi} \\ {}^{w}D_{ijk}^{\psi\phi\psi} \\ {}^{w}D_{ijk}^{\psi\psi\phi} \\ {}^{w}D_{ijk}^{\psi\psi\psi} \end{bmatrix} \tag{46}$$

and

$$\left[\epsilon_{ijk}^{-1}\right]_{\text{Haar}} = \mathbf{A}\left[\epsilon_{ijk}^{-1}\right]_{rec}\mathbf{A}. \tag{47}$$

The transformed matrix $[\epsilon_{ijk}^{-1}]_{\text{Haar}}$ can be reduced to a simple matrix having a highly symmetric representation

$$\begin{aligned}\left[\epsilon_{ijk}^{-1}\right]_{\text{Haar}} &= \mathbf{A}\left[\epsilon_{ijk}^{-1}\right]_{rec}\mathbf{A} \\ &= \begin{bmatrix} \alpha_1 & \alpha_2 & \alpha_3 & \alpha_4 & \alpha_5 & \alpha_6 & \alpha_7 & \alpha_8 \\ \alpha_2 & \alpha_1 & \alpha_5 & \alpha_6 & \alpha_3 & \alpha_4 & \alpha_8 & \alpha_7 \\ \alpha_3 & \alpha_5 & \alpha_1 & \alpha_7 & \alpha_2 & \alpha_8 & \alpha_4 & \alpha_6 \\ \alpha_4 & \alpha_6 & \alpha_7 & \alpha_1 & \alpha_8 & \alpha_2 & \alpha_3 & \alpha_5 \\ \alpha_5 & \alpha_3 & \alpha_2 & \alpha_8 & \alpha_1 & \alpha_7 & \alpha_6 & \alpha_4 \\ \alpha_6 & \alpha_4 & \alpha_8 & \alpha_2 & \alpha_7 & \alpha_1 & \alpha_5 & \alpha_3 \\ \alpha_7 & \alpha_8 & \alpha_4 & \alpha_3 & \alpha_6 & \alpha_5 & \alpha_1 & \alpha_2 \\ \alpha_8 & \alpha_7 & \alpha_6 & \alpha_5 & \alpha_4 & \alpha_3 & \alpha_2 & \alpha_1 \end{bmatrix}\end{aligned} \tag{48}$$

where the inner products

$$\alpha_i = \tfrac{1}{8}\mathbf{a}_i \cdot \mathbf{e}^{-1}, \quad \text{for } i = 1, 2, \cdots, 8 \tag{49}$$

with the column vectors $\mathbf{a}_i$ $(i = 1, \cdots, 8)$ and $\mathbf{e}^{-1}$ defined by

$$\mathbf{A} = [\mathbf{a}_1\, \mathbf{a}_2\, \mathbf{a}_3\, \mathbf{a}_4\, \mathbf{a}_5\, \mathbf{a}_6\, \mathbf{a}_7\, \mathbf{a}_8] \tag{50}$$

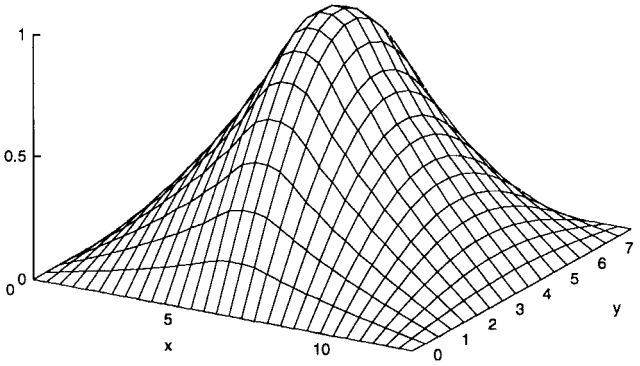

Fig. 17. An E_z field distribution of the centered-dielectric-slab loaded rectangular cavity shown in Fig. 6(b) at time step of 2389.

and

$$\mathbf{e}^{-1} = \left[\frac{1}{\epsilon_{ijk}^{lll}}\ \frac{1}{\epsilon_{ijk}^{llu}}\ \frac{1}{\epsilon_{ijk}^{lul}}\ \frac{1}{\epsilon_{ijk}^{ull}}\ \frac{1}{\epsilon_{ijk}^{luu}}\ \frac{1}{\epsilon_{ijk}^{ulu}}\ \frac{1}{\epsilon_{ijk}^{uul}}\ \frac{1}{\epsilon_{ijk}^{uuu}}\right]^{\dagger}. \tag{51}$$

In the time-stepping algorithm, (44) is computed after the flux density $\mathbf{D}$ is updated by (38).

A TE_{110} mode of the centered-dielectric-slab loaded rectangular cavity shown in Fig. 6(b) was analyzed with this formulation. The number of Yee cells used in the analysis was $14 \times 8 \times 6$ and nonuniform grids were incorporated. With Δt being 0.8 times the Courant limit, which was $\Delta t = 0.698$ ns, 2389 time steps were performed. The extensive computation showed that the exact formulation was stable at 10^6 time steps, and no instability was observed. The E_z field plot demonstrates smooth field distribution as shown in Fig. 17. Although this scheme takes longer computational time than the formulation described in Section II for the approximate treatment of inhomogeneous dielectric materials, it can be applied only at the dielectric interface to improve the computational efficiency.

VI. Conclusions

A three-dimensional multiresolution analysis procedure similar to the FDTD method has been derived by using three-dimensional Haar scaling and wavelet functions. The resulting method has been tested and validated by analyzing several cavity structures including inhomogeneously dielectric loaded rectangular cavities. The method has also been applied to the analysis of microwave passive structures such as microstrip low-pass filters and spiral inductors.

$$\left[\epsilon_{ijk}^{-1}\right]_{rec} = \begin{bmatrix} 1/\epsilon_{ijk}^{lll} & & & & & & & \\ & 1/\epsilon_{ijk}^{llu} & & & & & & \\ & & 1/\epsilon_{ijk}^{lul} & & & & & \\ & & & 1/\epsilon_{ijk}^{ull} & & & & \\ & & & & 1/\epsilon_{ijk}^{luu} & & & \\ & & & & & 1/\epsilon_{ijk}^{ulu} & & \\ & & & & & & 1/\epsilon_{ijk}^{uul} & \\ & & & & & & & 1/\epsilon_{ijk}^{uuu} \end{bmatrix} \tag{43}$$

The resulting S-parameters are in good agreement with those obtained with the conventional FDTD method. However, the field distribution plots show small distortions in the proposed method. The calculation time for the proposed method was approximately half that of the equivalent conventional FDTD method.

REFERENCES

[1] K. S. Yee, "Numerical solution of initial boundary value problems involving maxwell's equation in isotropic media," *IEEE Trans. Antennas Propagat.*, vol. AP-14, pp. 302–307, May 1966.

[2] W. J. R. Hoefer, "The transmission-line matrix method—Theory and applications," *IEEE Trans. Microwave Theory Tech.*, vol. MTT-33, pp. 882–893, Oct. 1985.

[3] I. Daubechies, *Ten Lectures on Wavelets.* Philadelphia, PA: SIAM, 1992.

[4] S. G. Mallat, "A theory for multiresolution signal decomposition: The wavelet representation," *IEEE Trans. Pattern Anal. Machine Intell.*, vol. 11, pp. 647–693, July 1989.

[5] B. Z. Steinberg and Y. Leviatan, "On the use of wavelet expansions in the method of moments," *IEEE Trans. Antennas Propagat.*, vol. 41, pp. 610–619, May 1993.

[6] M. Krumpholz and L. P. B. Katehi, "New prospects for time domain analysis," *IEEE Microwave Guided Wave Lett.*, vol. 5, pp. 382–384, Nov. 1995.

[7] ———, "MRTD: New time-domain schemes based on multiresolution analysis," *IEEE Trans. Microwave Theory Tech.*, vol. 44, pp. 555–571, Apr. 1996.

[8] M. Werthen and I. Wolff, "A novel wavelet based time domain simulation approach," *IEEE Microwave Guided Wave Lett.*, vol. 6, pp. 438–440, Dec. 1996.

[9] K. Goverdhanam, L. P. B. Katehi, and A. Cangellaris, "Application of multiresolution based FDTD multigrid," in *1997 IEEE MTT-S Int. Microwave Symp. Dig.*, pp. 333–336.

[10] K. Goverdhanam, E. Tentzeris, and L. P. B. Katehi, "Treatment of boundaries in multiresolution based FDTD multigrid," in *Proc. 14th Annual Review of Progress in Applied Computational Electromagnetics*, Mar. 1998, pp. 127–134.

[11] E. Tentzeris, R. Robertson, L. P. B. Katehi, and A. Cangellaris, "Space- and time-adaptive gridding using MRTD technique," in *1997 IEEE MTT-S Int. Microwave Symp. Dig.*, pp. 337–340.

[12] E. Tentzeris, M. Krumpholz, and L. P. B. Katehi, "Application of MRTD to printed transmission lines," in *1996 IEEE MTT-S Int. Microwave Symp. Dig.*, pp. 573–577.

[13] R. Robertson, E. Tentzeris, M. Krumpholz, and L. P. B. Katehi, "Modeling of dielectric cavity structures using multiresolution time-domain analysis," *Int. J. Numer. Model.*, vol. 11, pp. 55–68, 1998.

[14] K. L. Shlager and J. B. Schneider, "Analysis of the dispersion properties of the multiresolution time-domain (MRTD) scheme," in *Proc. IEEE AP-S Int. Symp. 1997*, pp. 2144–2147.

[15] D. H. Choi and W. J. R. Hoefer, "The finite-difference—time-domain method and its application to eigenvalue problems," *IEEE Trans. Microwave Theory Tech.*, vol. MTT-34, pp. 1464–1470, Dec. 1986.

[16] D. M. Sheen, S. M. Ali, M. D. Abouzahra, and J. A. Kong, "Application of the three-dimensional finite-difference time-domain method to the analysis of planar microstrip circuits," *IEEE Trans. Microwave Theory Tech.*, vol. 38, pp. 849–857, July 1990.

Masafumi Fujii (M'95–S'98) was born in Osaka, Japan, in 1966. He received the B.E. and M.E. degrees in electrical and electronic engineering from Kobe University, Hyogo, Japan, in 1989 and 1991, respectively. He is currently working toward the Ph.D. degree in electrical engineering at the University of Victoria, B.C., Canada.

He worked for Sumitomo Metal Industries, Ltd., Japan, where he was involved in numerical analysis of microwave components. His research interest is in the area of numerical analysis and modeling of electromagnetic fields using wavelet approximation.

Wolfgang J. R. Hoefer (M'71–SM'78–F'91) received the Dipl.-Ing. degree in electrical engineering from the Technische Hochschule Aachen, Germany, in 1965, and the D.Ing. degree from the University of Grenoble, France, in 1968.

From 1968 to 1969, he was a Lecturer at the Institut Universitaire de Technologie de Grenoble, France, and a Research Fellow at the Institut National Polytechnique de Grenoble, France. In 1969, he joined the Department of Electrical Engineering, University of Ottawa, Ottawa, Ont., Canada, where he was a Professor until March 1992. Since April 1992, he has held the NSERC/MPR Teltech Industrial Research Chair in RF Engineering, Department of Electrical and Computer Engineering, University of Victoria, B.C., Canada, and is a fellow of the Advanced Systems Institute of British Columbia. During sabbatical leaves in 1976 and 1977, he spent six months with the Space Division of AEG-Telefunken (now ATN) in Backnang, Germany, and six months with the Electromagnetics Laboratory of the Institut National Polytechnique de Grenoble. From 1984 to 1985, he was a Visiting Scientist at the Space Electronics Directorate of the Communications Research Center in Ottawa, Ont., Canada. From 1990 to 1991, he spent a third sabbatical year as a Visiting Professor at the Universities of Rome *Tor Vergata* in Italy, Nice-Sophia Antipolis in France, and TUM, Munich, Germany. His research interests include numerical techniques for modeling electromagnetic fields and waves, CAD of microwave and millimeter-wave circuits, microwave measurement techniques, and engineering education.

Dr. Hoefer is the co-founder and Managing Editor of the *International Journal of Numerical Modeling*, Associate Editor of the IEEE TRANSACTIONS ON MICROWAVE THEORY AND TECHNIQUES, and Chair of the MTT-15 Technical Committee on Microwave Field Theory.